J Mater Sci (2014) 49:7809–7818
DOI 10.1007/s10853-014-8491-x

Structural, electronic, and optical properties of orthorhombic and triclinic $BiNbO_4$ determined via DFT calculations

F. Litimein · R. Khenata · Sanjeev K. Gupta · G. Murtaza · Ali. H. Reshak · A. Bouhemadou · S. Bin Omran · Masood Yousaf · Prafulla K. Jha

Received: 7 March 2014 / Accepted: 18 July 2014 / Published online: 6 August 2014

Abstract We performed ab initio calculations using the FPLAW method with the local density approximation (LDA) implemented in the WIEN2 k code for the orthorhombic (α) and triclinic (β) phases of $BiNbO_4$. The modified Becke–Johnson exchange potential (mBJ)-LDA approach was also used to improve the electronic properties. The lattice constants calculated for both structures using the LDA are in good agreement with the experimental values. For the band structure calculations, the mBJ-LDA approach provides reasonable agreement for the band gap value compared with the LDA. The estimated (mBJ)-LDA band gap values are 2.89 eV (3.73 eV) and 2.62 eV (3.15 eV) for the α and β phases of $BiNbO_4$, respectively. Significant optical anisotropy is clearly observed in the visible-light region. We also calculated and evaluated the electron energy loss spectrum for $BiNbO_4$. This work provides the first quantitative theoretical prediction of optical properties and electron energy loss spectra for both the orthorhombic and triclinic phases of $BiNbO_4$.

Introduction

Bismuth niobate fourfold oxide ($BiNbO_4$) is an important material with a wide range of applications. This compound exists in two important crystalline phases (polymorphs): a low-temperature orthorhombic (α) and a high-temperature triclinic (β) [1–5]. Currently, photocatalysis has become an interesting topic of research for addressing environmental problems [1–7]. Previously developed photocatalysts have

F. Litimein
Laboratoire d'études des matériaux et instrumentations expérimentales, Université Djilali Liabes de Sidi Bel-Abbes, 22000 Sidi Bel Abbes, Algeria

R. Khenata
Laboratoire de Physique Quantique et de Modélisation Mathématique, Université de Mascara, 29000 Mascara, Algeria
e-mail: khenata_rabah@yahoo.fr

S. K. Gupta
Department of Physics, St. Xavier's College, Navrangpura 380009, Ahmedabad, India

G. Murtaza (✉)
Materials Modeling Laboratory, Department of Physics, Islamia College University, Peshawar, Pakistan
e-mail: murtaza@icp.edu.pk

Ali. H. Reshak
New Technologies - Research Center, University of West Bohemia, Univerzitni 8, 306 14 Pilsen, Czech Republic

Ali. H. Reshak
Center of Excellence Geopolymer and Green Technology, School of Material Engineering, University Malaysia Perlis, 01007 Kangar, Perlis, Malaysia

A. Bouhemadou
Laboratory for Developing New Materials and their Characterization, Department of Physics, Faculty of Science, University Setif 1, 19000 Setif, Algeria

S. Bin Omran
Department of Physics and Astronomy, College of Science, King Saud University, P.O. Box 2455, Riyadh 11451, Saudi Arabia

M. Yousaf
Physics Department, Faculty of Science, Universiti Teknologi Malaysia, 81310 Skudai, Johor, Malaysia

P. K. Jha
Department of Physics, M. S. University of Baroda, Vadodara 390002, India

wide band gaps in which photocatalytic activities are operational under UV light irradiation (band gap ~3.2 eV) and, thus, they have limited practical applications, as the solar spectrum is composed of only 4 % UV light. However, visible light constitutes 46 % of the total radiation emitted by the sun representing a more useful region in the solar spectrum. As a consequence, the synthesis of novel photocatalysts with the band gaps near the energy required to split water is of particular interest [8, 9].

Metal oxides continue to be promising candidates for the above goal because of their relative stability, low-cost processing technologies, and suitability for band gap engineering. Among metal oxides, the oxide $BiNbO_4$, along with other oxides containing the cation Bi, such as $BiVO_4$ [10–13], Bi_2WO_6 [14], $BiPO_4$ [15–17], Bi_2MoO_6 [18], $BiNbO_4$ [19–24], $BiTaO_4$ [25], Bi_4TaO_8I [26], $Bi_2O_2CO_3$ [27], and BiOX (X = Cl, Br or I) [28–32], has been found to have a significantly higher photocatalytic activity than the reference TiO_2. It has been reported that single-crystals $BiTa_{1-x}Nb_xO_4$ samples synthesized using a solid state reaction method can efficiently produce hydrogen and oxygen through water splitting under UV and visible light irradiation [19, 22]. Additionally, Zhai and coworkers recently investigated $BiNbO_4$ and $BiTaO_4$ powders and reported that $BiNbO_4$ has higher photocatalytic efficiency than $BiTaO_4$, which is ascribed to its large surface area and its more positive conduction band level [33]. Moreover, $BiNbO_4$ can also be used as a promising dielectric material, as it has a relatively low melting point. The literature indicates that the temperature coefficient for the resonant frequency, the dielectric constant, and the quality factor Q are ~50 ppm/°C, ~45 and 14000, respectively [34–39].

$BiNbO_4$ exists in two polymorphs: a low-temperature orthorhombic (α) phase [3–5] and a high-temperature triclinic (β) phase [1, 2, 19]. It has been found that the $BiNbO_4$ synthesized at 900 °C undergoes an irreversible phase transition from low-temperature orthorhombic to high-temperature triclinic (at 1293 K). Zhou et al. [40] reported a reversible phase transition from β → α in bulk ceramic samples; however, the transition was believed to be irreversible in powder samples until the recent work of Zhai et al. [33], in which the authors demonstrated that the phase transition from β to α-$BiNbO_4$ can occur in a $BiNbO_4$ powder system. Furthermore, Xu and coworkers [41] investigated the phase transitions of α-$BiNbO_4$ and β-$BiNbO_4$ under high pressure and high temperature (HPHT) (0–5 GPa and 300–1800 °C, respectively) using X-ray diffraction (XRD). The authors reported that below 3 GPa, β-$BiNbO_4$ is stable up to 1800 °C, while α-$BiNbO_4$ transforms to β-$BiNbO_4$ when the temperature exceeds 1150 °C.

There is abundant literature on the theoretical aspects on high-temperature phase studies for these materials; however, only a few studies have been performed for the low-temperature phase due to the restriction of its higher photocatalytic activity. Because the optical band gap of $BiNbO_4$ is approximately 2.6–2.8 eV [20–24, 33], larger than the required band gap (2.0 eV), research has shown that the effects of intrinsic defects [42] and co-doping [43, 44] can reduce the optical band gap, thus making $BiNbO_4$ a promising candidate as an efficient water-splitting photocatalyst. Thus, to understand the functional properties of both $BiNbO_4$ structures and to further optimize them, we must study their precise electronic and optical properties. Currently, the electronic structure and optical properties of this compound are not thoroughly understood. Structural relaxation, band structure, and total energy calculations have been performed for the pure orthorhombic phase of $BiNbO_4$ using the projector-augmented wave (PAW) method [42–44], but, to the best of our knowledge, there have been no studies reporting on calculations of their optical properties. In addition, calculations regarding the electronic structure and optical properties of the triclinic phase of $BiNbO_4$ are scarce. This lack of information has motivated us to study the electronic and optical properties of this compound in both forms.

Calculation details

All calculations presented in this work are based on the density functional theory (DFT) [45] combined with the full potential linearized augmented plane wave method, as implemented in the WIEN2 k code [46]. To perform calculations of the structural and electronic properties, we used the local density approximation (LDA) [47]. The recently developed modified Becke-Johnson exchange potential (mBJ) [48] is also used to improve the results for the electronic and optical properties. The valence electron configurations used in the calculations are $Bi(5d^{10}6s^26p^3)$, $Nb(4d^45\ s^1)$, and $O(2s^22p^4)$. In the present work, the wave function, charge density, and potential are expanded by spherical harmonic functions inside non-overlapping spheres surrounding the atomic sites (muffin-tin spheres) and by a plane wave basis set in the remaining space of the unit cell (interstitial region). The maximum quantum number l for the wave function expansion within the atomic spheres is confined to $l_{max} = 10$. The Fourier-expanded charge density was truncated at $G_{max} = 14$ $(Ry)^{1/2}$, where G_{max} represents the largest Fourier expansion vector. The plane-wave cutoff which controls the size of the basis, defined by the product of the smallest atomic sphere radius times the magnitude of the largest reciprocal-lattice vector ($RMT_{min}.K_{max}$), was set to 8.0. The muffin-tin radii were set to 2.02, 1.87, and 1.65 atomic units (a.u) for Bi, Nb, and O, respectively. For a band structure

representation, we chose up to 50 ***k***-points for any high-symmetry direction. Dense meshes of 1200 ***k***-points (for the orthorhombic structure) and 1000 ***k***-points (for the triclinic structure) were generated in the irreducible part of the Brillouin zone (BZ) to compute the total and projected DOS as well as the dipole matrix elements.

The optical properties of the material are determined from the complex dielectric function $\varepsilon(\omega) = \varepsilon_1(\omega) + i\,\varepsilon_2(\omega)$. The imaginary part $\varepsilon_2(\omega)$ was calculated from the momentum matrix elements between the occupied and unoccupied wave functions within the selection rules while the real part $\varepsilon_1(\omega)$ of the dielectric function can be evaluated from the imaginary part of the dielectric function using the Kramers–Kronig relationship. There are two contributions to $\varepsilon(\omega)$, namely, the intraband and interband transitions. The intraband transition corresponds to electronic conduction due to free carriers, and is hence more important in conducting materials such as metals, semimetals, and degenerate semiconductors. The interband transition, which is divided into a direct and an indirect transition, corresponds to the absorption of electromagnetic radiation by an electron in an occupied state below the Fermi level, thereby inducing a transition to an unoccupied state in a higher band. Here we neglect indirect transitions that involve the absorption or emission of a phonon. Furthermore, all solid macroscopic optical constants such as the refractive index $n(\omega)$, extinction coefficient $k(\omega)$, optical reflectivity $R(\omega)$, and energy-loss spectrum $L(\omega)$ can be computed from $\varepsilon_2(\omega)$.

Results and discussion

Structural properties

The low-temperature orthorhombic (α) and high-temperature triclinic (β) structures are shown in Fig. 1. Both structures have four formula units. The NbO_6 octahedra are joined by four vertices to form sheets of $[NbO_4]_n$ with some distortion. The α structure, which is orthorhombic with the space group *Pnna* (No. 52), consists of layers of vertices and sites that are shared with NbO_6 that are normal to the *c*-plane. The Bi^{3+} atoms are located at the sites between these layers. The triclinic $BiNbO_4$ structure, which is the most suitable phase for most high-temperature applications, belongs to the P_1 space group. This form consists of pseudo layers of interconnected $[Bi_2O_2]$ units surrounded by sheets of $[NbO_4]_n$ along the *bc*- plane. The experimental unit-cell parameters are determined and subsequently verified by single-crystal X-ray techniques and the resulting structural refinements for both the orthorhombic [3, 5, 21, 23, 24], and triclinic [1, 2, 19] phases.

The relaxed lattice parameters for both the α- and β-single-crystal phases are presented in Table 1 and 2, respectively, and are compared with previous experimental and theoretical findings [5, 44]. We note that the first attempt toward a structural determination of the high-temperature triclinic form of $BiNbO_4$ was reported by Keve and Skapski, using single-crystal X-ray techniques. The authors obtained crystallographic data for the $P\ \bar{1}$ space group with $a = 7.61(1)$Å, $b = 5.53(6)$Å, $c = 7.91(9)$Å, $\alpha = 89.88°$, $\beta = 77.43°$, $\gamma = 87.15°$, and $Z = 4$ [2]. Our calculated lattice parameters and unit cell volume for β-$BiNbO_4$ are compared with the experimental single-crystal X-ray diffraction data recently reported by Muktha et al. [19]. For the orthorhombic phase, our results are compared to the crystallographic data of Subramanian et al. [5]. Our computed *a* and *b* lattice parameters for α-$BiNbO_4$ are underestimated by 5 and 8 %, respectively, which is consistent with the general trend of the LDA. The computed lattice parameter *c* is in excellent agreement with the experimental data. The LDA unit cell volume is smaller by 1.28 % in comparison to the experimental data. Similarly, for the triclinic structure, the LDA approach tends to underestimate the interatomic distances and unit cell size, with the lattice parameters *a*, *b*, and *c* being smaller than the experimental values by 1.32, 1.67, and 2.09 %.

Electronic properties

This subsection provides a study of the electronic structure of both the orthorhombic and triclinic phase of $BiNbO_4$ with the local density approximation (LDA) as well as the modified BJ approximation (TB-mBJ) implemented in the WIEN2k code. The electronic structure is an important quantity dominating the material's properties, and its study is necessary to bridge the relationship between the material structure and properties.

The band structures of both phases of $BiNbO_4$ along the high-symmetry directions in the first Brillouin zone (BZ) are calculated at the equilibrium volume with the LDA and mBJ-LDA approximations and not presented here. It is well known that mBJ-LDA produces band gap values in close agreement with experimentally measured values. The zero energy is chosen to coincide with the top of the valence band. It is to be noted that the band structure of the orthorhombic structure is determined according to the orthorhombic Brillouin zone [42] and the electron dispersion curves of the triclinic structure are determined along nine different symmetry directions in the BZ [49]. It is observed from the calculations of the band structure of the compound that there is an overall topological similarity between the orthorhombic band structure and those calculated in previous studies [42]. For the triclinic structure, there are no previous band structure calculations to use for comparison.

In view of Table 3, it is noted that for the orthorhombic structure, the conduction band minimum (CBM) is located

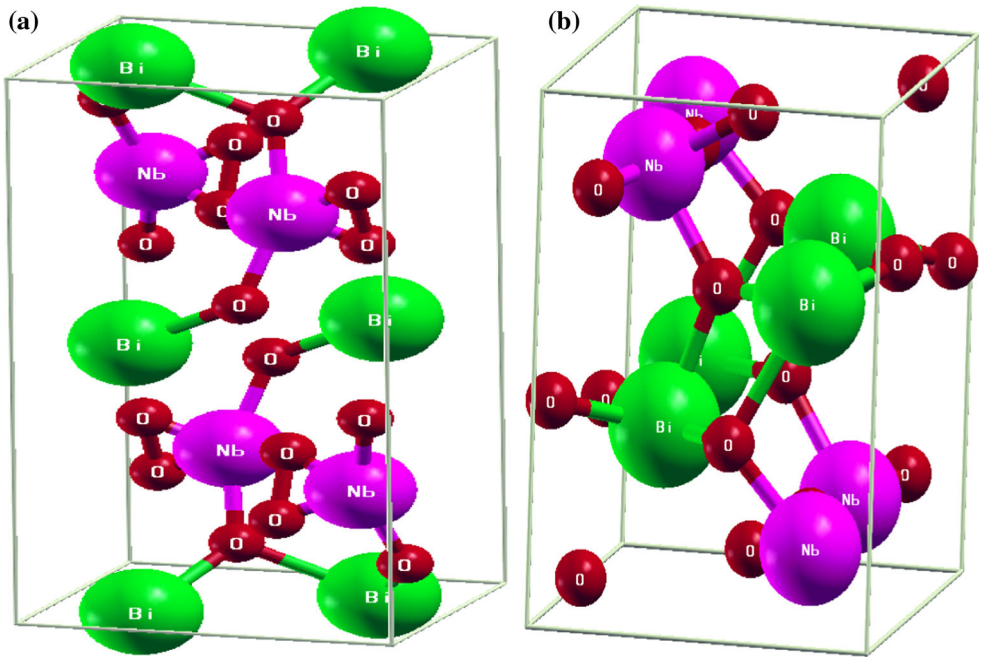

Fig. 1 Schematic illustration of crystalline structures for α-$BiNbO_4$ (**a**) and β-$BiNbO_4$ (**b**)

along the T-Y line of the BZ while the valence band maximum (VBM) occurs along the Y-Γ line of the BZ, resulting in an indirect band gap (E_g = 3.73 eV). For the triclinic phase both CBM and VBM are located at the Γ-point, resulting in a direct band gap (E_g = 3.153 eV). The fundamental energy band gap values for both the orthorhombic and triclinic phases of $BiNbO_4$ are summarized in Table 4. The calculated mBJ band gap values agree well with the experimental data presented in Refs. [50–52]. The disagreement with some experimental band gap values is due to the use of different methods and the nature of the compound, as either a powder or a bulk samples. According to the results of Wiegel and co-workers, the indirect band gap E_g should be 3.5 and 3.75 eV for β- $BiNbO_4$ and α- $BiNbO_4$, respectively. The mBJ-LDA approach is employed here as a possible alternative to accurately model the energy band gap of both polymorphs of $BiNbO_4$, giving results very close to the experimental values shown in Table 4.

The main difference between the LDA and mBJ-LDA results is a shift factor that systematically increases the energy band gap value in the mBJ calculations. Our LDA results give a band gap of 2.94 eV for α-$BiNbO_4$ and 2.62 eV for β-$BiNbO_4$. The calculations of Lai et al. [42] based on the GGA approximation for α -$BiNbO_4$ gave an energy band gap of 2.87 eV which is in good agreement with our value. However, our calculated LDA values are in much better agreement with the experimental data estimated by Zou et al. [22–24], Dunkle et al. [20] and Zhai et al. [33] for the orthorhombic phase of $BiNbO_4$.

Table 1 Calculated unit cell parameters and bulk modulus at zero-pressure for the β and α phases of $BiNbO_4$. Experimental and theoretical values are included for comparison

Phase	Property	Present work	Other work[a]	Expt.
α -$BiNbO_4$	*a* (Å)	5.63713	5.715	5.673[b]
	b (Å)	11.6326	11.623	11.714[b]
	c (Å)	4.973	5.001	4.978[b]
	B (GPa)	201.15		
	B′	4.52		
β-$BiNbO_4$	*a* (Å)	5.4745		5.5376[c]
	b (Å)	7.5899		7.6184[c]
	c (Å)	7.8972		7.9324[c]
	α (°)	102.54		102.565[c]
	β (°)	90.0164		90.143[c]
	γ (°)	92.852		92.788[c]
	B (GPa)	206.14		
	B′	4.553		

[a] Reference [44]

[b] Reference [5]

[c] Reference [19]

Density of states (DOS) plots for α-$BiNbO_4$ and β-$BiNbO_4$ are shown in Figs. 2 and 3, respectively. In an effort to obtain more exact information on the atom-specific character of each band, the DOS was further decomposed into the atom orbital (AO)-projected DOS (PDOS) in terms of the atomic and angular momentum contributions. The general features for α-$BiNbO_4$ and β-$BiNbO_4$ are very similar. In both structures, the valence bands (VBs) are divided in three regions. The energetically lower part of the

Table 2 Calculated LDA atomic positions for the orthorhombic phase (space group Pnna (No.52), Z = 2) and triclinic phase (space group $P\bar{1}$ (No. 2), Z = 4) of $BiNbO_4$. Experimental values are included for comparison

Atom	Wyckoff site	Ab initio LDA			X-ray diffraction		
		x	*Y*	*z*	*x*	*y*	*z*
α-$BiNbO_4$[a]							
Bi(1)	4*i*	0.2500	0.5000	0.7793	0.2500	0.5000	0.7813
Nb(1)	4*i*	0.3574	0.2500	0.2500	0.3478	0.2500	0.2500
O(1)	4*i*	0.1457	0.3052	0.5068	0.1396	0.3052	0.5039
O(2)	4*i*	0.41897	0.0982	0.4135	0.4139	0.0985	0.4136
β -$BiNbO_4$[b]							
Bi(1)	2*i*	0.28512	0.83286	0.62391	0.28062	0.83463	0.62529
Bi(2)	2*i*	0.23442	0.87721	0.12766	0.23707	0.87647	0.12599
Nb(1)	2*i*	0.22290	0.34274	0.18022	0.22503	0.34402	0.17940
Nb(2)	2*i*	0.24625	0.32619	0.67997	0.24367	0.32513	0.67849
O(1)	2*i*	0.00434	0.10559	0.17820	0.0026	0.1027	0.1774
O(2)	2*i*	0.44386	1.10709	0.67569	0.4439	1.1055	0.6744
O(3)	2*i*	0.15754	0.31808	0.94543	0.1626	0.3185	0.9471
O(4)	2*i*	0.07985	0.55311	0.72802	0.0788	0.5518	0.7312
O(5)	2*i*	0.30054	0.32789	0.44945	0.2985	0.3286	0.4514
O(6)	2*i*	0.43793	0.54645	0.21906	0.4359	0.5466	0.2203
O(7)	2*i*	0.46175	0.15409	0.14518	0.4642	0.1549	0.1472
O(8)	2*i*	0.04026	0.82978	0.36303	0.0389	0.8329	0.3616

[a] Reference [5]

[b] Reference [19]

valence bands (VBs) ranges from −18.2 to −15 eV primarily results from O-2 s states with minor contributions from the Nb-5p states. The middle region of the VB (−10.3 to −7.9 eV) primarily arises from Bi-6 s states. The lower band in the upper valence band, lying in the region between the top of the valence band down to about −5.5 eV, is due to near equal contribution of Nb-4d and O-2p states, while the higher energy band closest to the Fermi level is mainly due to O-2p states with minor contribution of Bi-6 s states. The lower part of the conduction band (CB) results from Bi-6p and O-2p antibonding states. The above results seem to be in good agreement with those obtained in DFT calculations of electronic properties using projector-augmented wave (PAW) method [42–44].

The electronic charge density distribution is a qualitative approach for investigating the interactions between the atoms. Therefore, we have investigated the electronic charge density in (101) crystallographic plane to describe the bonding properties of the α-$BiNbO_4$ and β-$BiNbO_4$. Fig. 4a, b illustrates the electronic charge density contour in (1 0 1) crystallographic plane which represents only Bi and O atoms for α-$BiNbO_4$ while it represents all atoms for β-$BiNbO_4$. In both compounds, O atoms form strong ionic bonding and show very weak covalent bonding with Bi atoms. In β-$BiNbO_4$ compound, the O atoms exhibit weak covalent bonding with Nb atoms. The bonding forms depending on Pauling electro-negativity difference of Bi (2.02), Nb (1.6), and O (3.44) atoms. Since O atoms possess higher electronegativity, therefore, it attracts the electrons. From the contour plots, one can see that the majority of Nb and Bi electronic charge is transferred to O atom, as it is clear from Fig. 4a, b the O atoms surrounding by a circle of blue color which corresponds to the maximum charge (+1.0000) according to the thermal charge density scale. The charge around O atom is uniformly

Table 3 Band gap energies (in eV) of orthorhombic α -$BiNbO_4$ and triclinic β -$BiNbO_4$ along selected high symmetry directions

	LDA		mBJ-LDA
α -$BiNbO_4$			
Γ- Γ	**2.94**	**Γ- Γ**	**3.73**
Γ-Z	3.29	Γ-Z	4.15
Γ-T	3.04	Γ-T	4.04
Γ-Y	3.10	Γ-Y	3.84
Γ-S	3.45	Γ-S	4.29
Γ-X	3.12	Γ-X	4.08
Γ-U	2.97	Γ-U	3.82
Γ-R	3.08	Γ-R	3.90
β -$BiNbO_4$			
Y–T	2.98	Γ –T	3.45
Y–Y	2.68	Γ-Y	3.25
Y- Γ	**2.62**	**Γ- Γ**	**3.15**
Y–Z	2.85	Γ-Z	3.37
Y-V	2.71	Γ-V	3.24
Y-X	2.84	Γ-X	3.30
Y-R	3.02	Γ-R	3.56

Bold values indicate the minimum energy bandgap

Table 4 Band gaps (in eV) calculated for different exchange–correlation potentials, compared with experimental data

	LDA	mBJ-LDA	Expt.
α-$BiNbO_4$	2.89	3.73	2.6[a], 2.8[b], 2.79[c], 3.5[d], 3.5[e]
β -$BiNbO_4$	2.62	3.153	3.39[f], 3.75[e]

[a] Reference [24]. Polycrystalline samples synthesized by a solid-state reaction method

[b] Reference [20]. Band gap of α-$BiNbO_4$ powder estimated from the absorption edge obtained by diffuse reflectance measurements

[c] Reference [33]. Optical gap calculated from UV–vis absorption data of $BiNbO_4$ powders calcined at 700 °C

[d] Reference [50]. Optical band gap determined by the Kubelka–Munk function

[e] Reference [51]

[f] Reference [52]

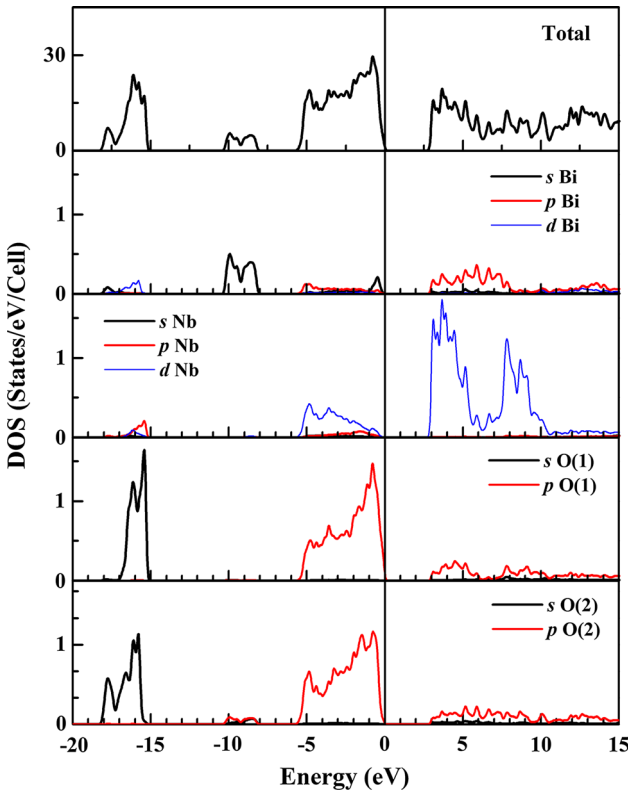

Fig. 2 Total and projected density of states of α -$BiNbO_4$. The Fermi energy is set to zero

distributed. Following Fig. 4 one can conclude that both of α-$BiNbO_4$ and β-$BiNbO_4$ exhibit strong ionic bonding and weak covalent bonding.

Optical properties

Calculations of the real and imaginary parts for the two phases of $BiNbO_4$ for different incident light polarizations ([1 0 0], [0 1 0] and [0 0 1], with respect to the crystalline

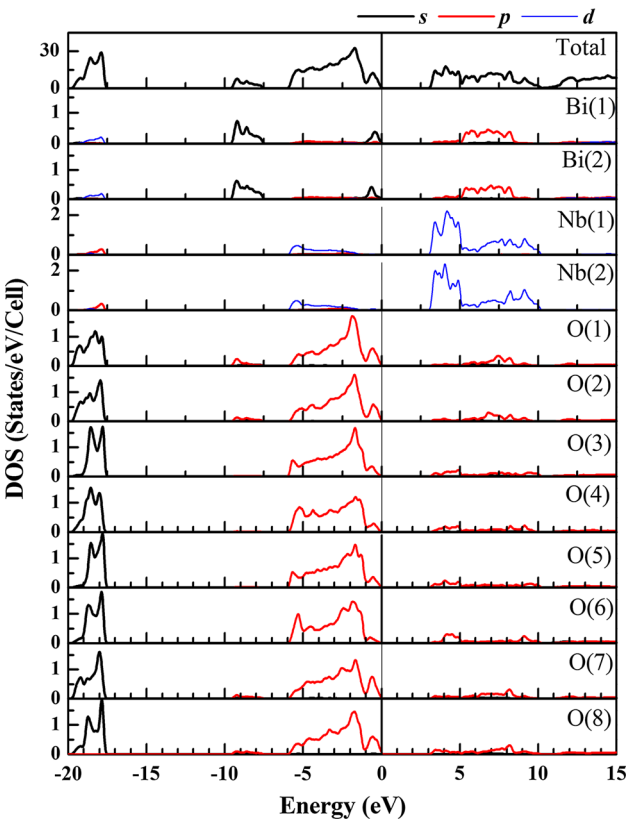

Fig. 3 Total and projected density of states of β–$BiNbO_4$. The Fermi energy is set to zero

axes), performed at the level of TB-mBJ, are displayed in Fig. 5a, b as a function of incident photon energy up to 45 eV. We note that only direct transitions which conserve the crystal momentum are included in our optical property calculations. Indirect transitions such as those assisted by lattice vibrations are excluded and found to have very small effect on the absorption edge. Lorentzian broadening is taken to be 0.3 eV.

The $\varepsilon_2(\omega)$ spectra can be divided in two energy regions corresponding to energies below and above 5.0/7.0 eV for the α/β polymorphs of $BiNbO_4$. For energies below 5.0/7.0 eV in the α/β polymorphs, the ε_2 (ω) spectra show that the first critical points (threshold energy) of the dielectric function occur at about 3.8/3.1, 3.54/3.0, and 3.7/2.82 eV along the [1 0 0], [0 1 0], and [0 0 1] directions, respectively. These points are the direct optical transitions between the highest valence band and the lowest conduction, which known as the fundamental absorption edge. Our calculated results show that the direct optical gap is larger than the smallest indirect band gap. For energies above 5.0 eV, the region of absorption peaks exhibits significant polarization anisotropy for both polymorphs, where the transitions primarily occur from the O-2p valence states to the Nb-4d conduction states, and shows an abrupt increase in the absorption intensity. The pattern of the dielectric

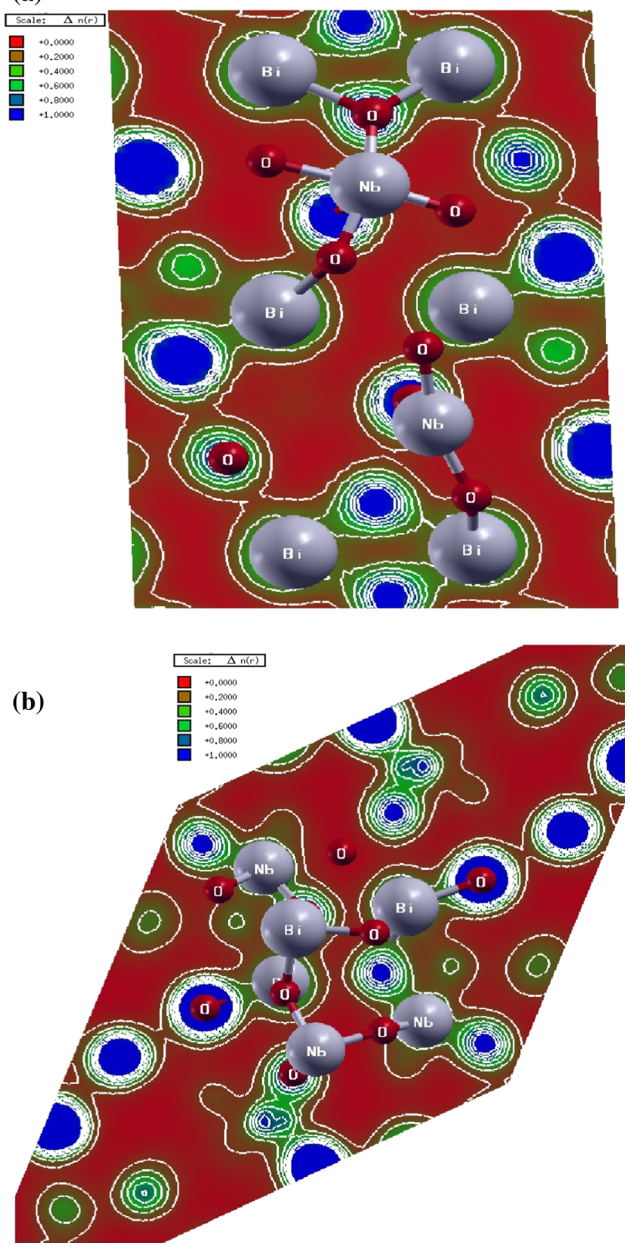

Fig. 4 2D contour plot for the total charge density distribution for α -$BiNbO_4$ (**a**) and β -$BiNbO_4$ (**b**) along the (101) crystallographic plane

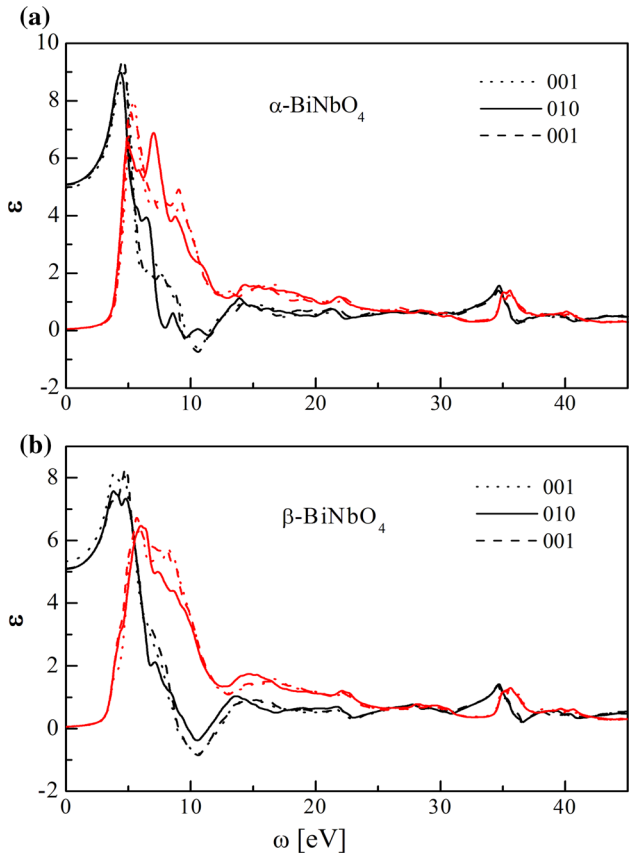

Fig. 5 Real part $\varepsilon_1(\omega)$ (*black line*) and imaginary part $\varepsilon_2(\omega)$(*red line*) of the complex dielectric function $\varepsilon(\omega)$ for three different polarizations of incident radiations (Color figure online)

Table 5 Optical dielectric constant, refractive index, and reflectivity of α-$BiNbO_4$ and β-$BiNbO_4$ at zero frequency

	α- $BiNbO_4$		β-$BiNbO_4$	
	LDA	mBJ-LDA	LDA	mBJ-LDA
ε_{xx}	6.539	4.9787	7.076	5.339
ε_{yy}	6.813	5.099	6.687	5.0899
ε_{zz}	6.6	5.078	6.728	5.109
$\bar{\varepsilon}$	6.651	5.052	6.830	5.179
$\bar{n}$	2.581	2.2476	2.613	2.275
$\bar{R}$	0.195	0.1476	0.1967	0.1517

functions spectra is almost similar for both the orthorhombic and triclinic phase of $BiNbO_4$ at low energy part ranging from 0.0 to 5.0 eV. At high energies, the dielectric functions for the α/β polymorphs of $BiNbO_4$ show a different pronounced peaks situated at 5.42/5.67 and 9.29/7.87 eV in the [1 0 0] direction; 5.83/6.05, 7.0/7.36, and 8.75/8.56 eV in the [0 1 0] direction; and 5.13/5.97, 9.07/8.20 eV in the [0 0 1] direction. In general, the optical absorption, as a function of the electric field alignment with respect to the crystalline axes, is more intense in the [0 1 0] crystal direction compared to the other directions.

The real parts of the dielectric function $\varepsilon_1(\omega)$ presented in Fig. 5 reflect several features of the imaginary parts due to the Kramers–Kronig relation. The vanishing frequency value in the dielectric function defines the static electronic dielectric constant $\varepsilon_1(0)$ for the α/β polymorphs of $BiNbO_4$. According to the results presented in the Fig. 5, the static dielectric constants are found to be approximately 5.05 for the α-$BiNbO_4$ phase and 5.18 for β-$BiNbO_4$, based on calculations with the mBJ approach. These values approach the experimental dielectric constant of 4.4 [53]. From

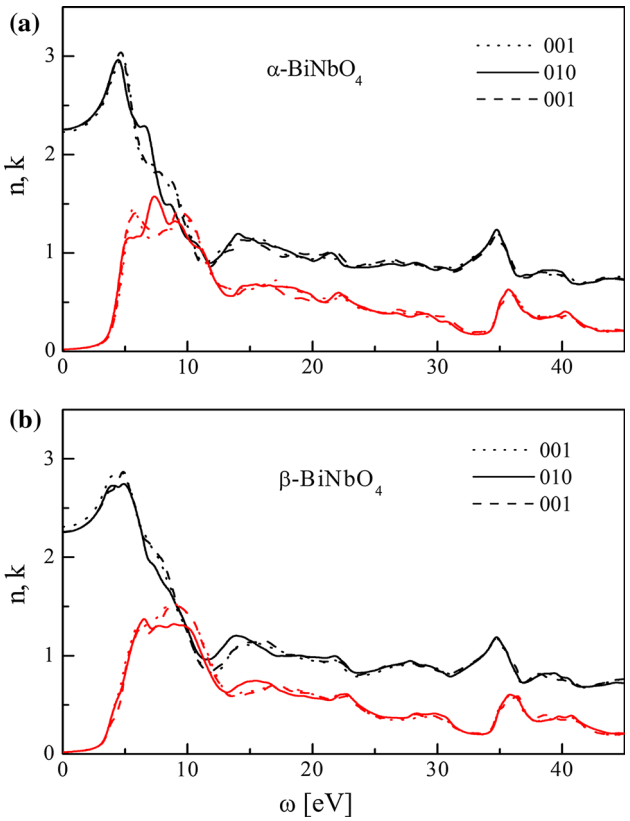

Fig. 6 Refractive index$n(\omega)$ (*black line*) and extinction coefficient $k(\omega)$ (*red line*) of α -$BiNbO_4$ (**a**) and β -$BiNbO_4$ (**b**) (Color figure online)

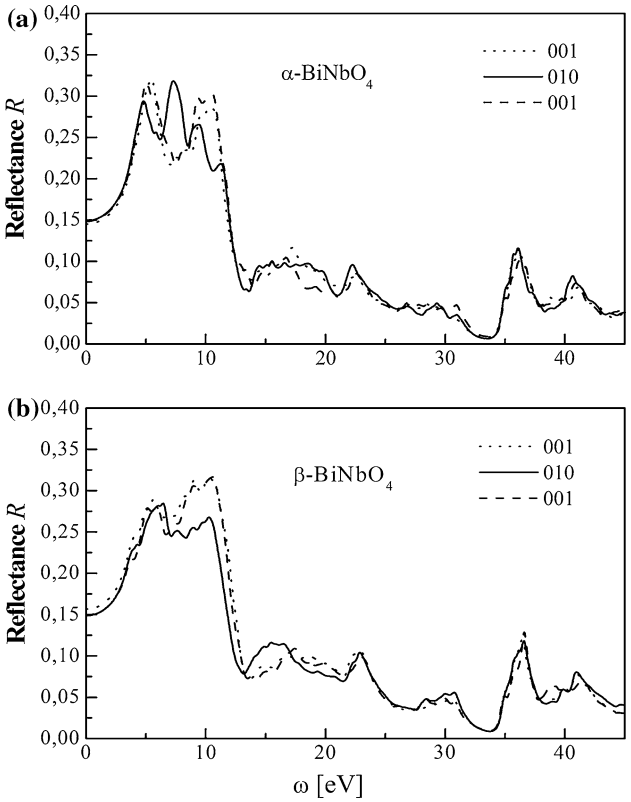

Fig. 7 The reflectivity $R(\omega)$ spectra of α -$BiNbO_4$ (**a**) and β -$BiNbO_4$ (**b**)

Table 5, one can see that the LDA calculations predict a much larger static dielectric constant of 6.65/6.83 for the α/β polymorphs. This result arises from an underestimation of the fundamental band gaps for calculations based on the LDA theory.

Figure 6 shows the behavior of the refraction index and the extinction coefficient, as a function of energy, along the [1 0 0], [0 1 0] and [0 0 1]-directions for both phases of $BiNbO_4$. The mean values of the static refractive index $n(0)$, which represents an informative quantity, are represented in Table 5. Our computed static refractive index $n(0)$ values compare well with the measured data reported by Popolitov et al. for α-$BiNbO_4$ [53] and by Tsujimi et al. [54] for β-$BiNbO_4$, corresponding to 2.5 and 2.2, respectively. The refractive index reaches a maximum value of 3.04 at 4.64 eV for the orthorhombic phase. For the triclinic phase maximum value of the refractive index is 2.87 at 4.86 eV. The extinction coefficient $k(\omega)$ was calculated for both phases, as shown in Fig. 6.

Fig. 7 displays the reflectivity spectra for both the orthorhombic and triclinic phases. From the extinction coefficient and reflectivity plots, one can define the absorption, reflection, and transparent regions [55]. The peak of the extinction coefficient represents absorption, and the peak of reflection indicates reflection. The regions in which both the extinction and reflectivity decrease correspond to transparent region. Based on this figure, these properties are approximately the same for the two phases. The energy values are less than 3 eV for both structures in the transparent region. The maximum values lie in the energy range of 3.5–11.52 eV for α-$BiNbO_4$ and 3.14–12 eV for β-$BiNbO_4$ which arises from the interband transition. Meanwhile, the minimum reflectivity occurs in the energy range above 13.75 eV for α-$BiNbO_4$ and 13.85 eV for β-$BiNbO_4$ due to the collective plasma resonance. The depth of the plasma resonance can be determined by the imaginary part of the dielectric function.

The electron energy loss spectra L(ω) can aid in describing the energy loss of a fast electron traversing in a material. Fig. 8 presents the result of the electron energy loss function for both $BiNbO_4$ polymorphs. Well-defined average maxima can be observed in the calculated energy loss spectrum at 8.36/7.08, 12.09/12.72, 20.04/20.99, 23.36/23.55, 27.22/28.5, 29.54, and 30.98/30.89 eV. The peak at 11.85/12.05 eV represents a plasmon resonance, as can be confirmed by Fig. 5. The real part of the dielectric function, which is identified by the point at which the function crosses the energy axis with a positive slope,

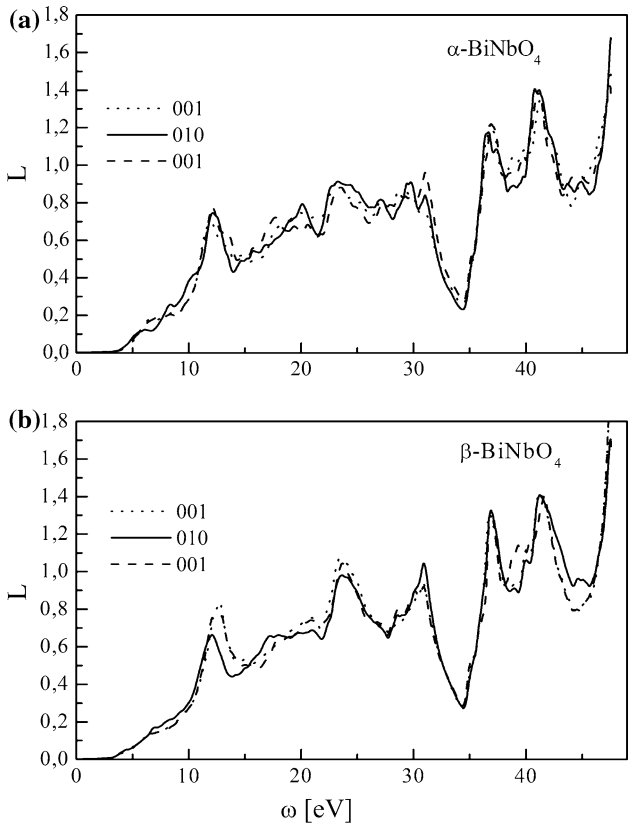

Fig. 8 Electron energy loss spectra $L(\omega)$ of α -$BiNbO_4$ (**a**) and β -$BiNbO_4$ (**b**)

indicates the presence of a well-defined plasmon signal at 12.09 eV. The other maxima in the energy loss function arise from interband transitions, such as the peaks observed in Fig. 5, and those from the imaginary part of the dielectric function $\varepsilon_2(\omega)$, as listed above.

Conclusions

We performed a first-principles study on $BiNbO_4$ in the orthorhombic and triclinic phases, calculating their structural, electronic, and optical properties. Using the mBJ-LDA approach, our FP-LAPW calculations predict that $BiNbO_4$ should be a direct-gap material in the triclinic phase and an indirect-gap material in the orthorhombic phase. Analysis of the PDOS reveals that the main contributions in the valence band arise from the O-2p, Bi-6 s/6p, and Nb-4d like states. In particular, the Bi 2p- and Nb 4d-like states primarily contribute at the bottom while the Bi 6 s- and O 2p-like states contribute at the top of the valence band of $BiNbO_4$, with contributions of the above states occurring throughout the entire valence-band region. Furthermore, our calculations indicate that the conduction band of $BiNbO_4$ is dominated by contributions from the Nb 4d- and Bi 6p-like states, with a small contribution from the O 2p-like states. The dielectric function, refractive index, extinction coefficient, reflectivity spectrum, and electron energy loss are calculated for photon energies up to 40 eV, and our calculations have provided assignments for several peaks associated with the interband transitions in both structures.

Acknowledgements R. K. and S. B.O acknowledge support from the National Plan for Science, Technology and Innovation under research project No. 11-NAN1465-02. A. H. R. developed results within the CENTEM project, reg. no. CZ.1.05/2.1.00/03.0088, co-funded by the ERDF as part of the Ministry of Education, Youth and Sports OPRDI program. S.K.G. acknowledges support from the Fulbright-Nehru Postdoctoral Research Fellowship and Department of Science and Technology (DST), Govt. of India. P.K.J. acknowledges the University Grants Commission (UGC) and the Department of Science and Technology (DST), Govt. of India.

References

1. Aurivillius B (1951) X-ray Investigations on $BiNbO_4$, $BiTaO_4$ and $BiSbO_4$. Ark Kemi 3:153–161
2. Keve ET, Skapski AC (1973) The crystal structure of triclinic β-$BiNbO_4$. J Solid State Chem 8:159–165
3. Roth RS, Waring JL (1962) Phase equilibrium relations in the binary system bismuth sesquioxide-niobium pentoxide. J Res Nat Bur Stand 66A:451–463
4. Roth RS, Waring JL (1963) Synthesis and stability of Bismutotantalite, Stibiotantalite and chemically similar ABO_4 compounds. Am Mineral 48:1348–1356
5. Subramaian MA, Calabrese JC (1993) Crystal structure of the below temperature form of Bismuth Niobium oxide [ct-$BiNbO_4$]. Mater Res Bull 28:523–529
6. Choi W, Hong SJ, Chang YS, Cho Y (2000) Photocatalytic degradation of polychlorinated dibenzo-*p*-dioxins on Tio_2 film under UV or solar light irradiation. Environ Sci Technol 34:4810–4815
7. Kudo A (2007) Photocatalysis and solar hydrogen production. Pure Appl Chem 79:1917–1927
8. Zhu J, Zach M (2009) Nanostructured materials for photocatalytic hydrogen production. Curr Opin Colloid Interface Sci 14:260–269
9. Hernandez-Alonso MD, Fresno F, Suarez S, Coronado JM (2009) Development of alternative photocatalysts to TiO_2: challenges and opportunities. Energy Environ Sci 2:1231–1257
10. Zhang J, Cui H, Wang B, Li C, Zhai J, Li Q (2013) Fly ash cenospheres supported visible-light-driven $BiVO_4$ photocatalyst: synthesis, characterization and photocatalytic application. Chem Eng J 223:737–746
11. Kohtani S, Makino S, Kudo A, Tokumura K, Ishigaki Y, Matsunaga T, Nikaido O, Hayakawa K, Nakagaki R (2002) Photocatalytic degradation of 4-n-Nonylphenol under irradiation from solar simulator: comparison between $BiVO_4$ and TiO_2 photocatalysts. Chem Lett 31:660–661
12. Zhang A, Zhang J, Cui N, Tie X, An Y, Li L (2009) Effects of pH on hydrothermal synthesis and characterization of visible-light-driven $BiVO_4$ photocatalyst. J Mol Catal A 304:28–32
13. Guo Y, Yang X, Ma F, Li K, Xu L, Yuan X, Guo Y (2010) Additive-free controllable fabrication of bismuth vanadates and their photocatalytic activity toward dye degradation. Appl Surf Sci 256:2215–2222

14. Fu HB, Pan CS, Yao WQ, Zhu YF (2005) Visible-light-induced degradation of rhodamine B by nanosized BI_2WO_6. J Phys Chem B 109:22432–22439
15. Kudo A, Omori K, Kato H (1999) A novel aqueous process for preparation of crystal form-controlled and highly crystalline $BiVO_4$ powder from layered vanadates at room temperature and its photocatalytic and photophysical properties. J Am Chem Soc 121:11459–11467
16. Pan C, Zhu Y (2010) New type of $BiPO_4$ oxy-acid salt photocatalyst with high photocatalytic activity on degradation of dye. Environ Sci Technol 44:5570–5574
17. Pan C, Zhu Y (2011) Size-controlled synthesis of $BiPO_4$ nanocrystals for enhanced photocatalytic performance. J Mater Chem 21:4235–4241
18. Yin WZ, Wang WZ, Sun SM (2010) Photocatalytic degradation of phenol over cage-like Bi_2MoO_6 hollow spheres under visible-light irradiation. Catal Commun 11:647–650
19. Muktha B, Darriet J, Madras G, Row TNG (2006) Crystal structures and photocatalysis of the triclinic polymorphs of $BiNbO_4$ and $BiTaO_4$. J Solid State Chem 179:3919–3925
20. Dunkle SS, Suslick KS (2009) Photodegradation of $BiNbO_4$ powder during photocatalytic reactions. J Phys Chem Lett C 113:10341–10345
21. Lee CY, Macquart R, Zhou Q, Kennedy BJ (2003) Structural and spectroscopic studies of $BiTa_{1-x}Nb_xO_4$. J Solid State Chem 174:310–318
22. Zou Z, Ye J, Sayama K, Arakawa H (2001) Photocatalytic and photophysical properties of a novel series of solid photocatalysts, $BiTa_{1-x}Nb_xO_4$ ($0 \leqslant x \leqslant 1$). Chem Phys Lett 343:303–308
23. Zou Z, Arakawa H, Ye J (2002) Substitution effect of Ta^{5+} by Nb^{5+} on photocatalytic, photophysical, and structural properties of $BiTa_{1-x}Nb_xO_4$ ($0 \leq x \leq 1.0$). J Mater Res 17:1446–1454
24. Zou Z, Ye JH, Arakawa H (2001) Optical and structural properties of the $BiTa_{1-x}Nb_xO_4$ ($0 \leq x \leq 1$) compounds. Solid State Commun 119:471–475
25. Ullah R, Sun H, Ang HM, Tadé MO, Wang S (2012) Photocatalytic oxidation of water and air contaminants with metal doped $BiTaO_4$ irradiated with visible light. Catal Today 192:203–212
26. Fan J, Hu XY, Xie ZG, Zhang KL, Wang JJ (2012) Photocatalytic degradation of azo dye by novel Bi-based photocatalyst Bi_4TaO_8I under visible-light irradiation. Chem Eng J 179:44–51
27. Xu YS, Zhang WD (2013) Anion exchange strategy for construction of sesame-biscuit-like $Bi_2O_2CO_3/Bi_2MoO_6$ nanocomposites with enhanced photocatalytic activity. Appl Catal B 140–141:306–316
28. Zhang KL, Liu CM, Huang FQ, Zheng C, Wang WD (2006) Study of the electronic structure and photocatalytic activity of the BiOCl photocatalyst. Appl Catal B 68:125–129
29. Wang W, Huang F, Lin X (2007) xBiOI–$(1-x)$BiOCl as efficient visible-light-driven photocatalysts. Scr Mater 56:669–672
30. Wang W, Huang F, Lin X, Yang J (2008) Visible-light-responsive photocatalysts xBiOBr–$(1-x)$BiOI. Catal Commun 9:8–12
31. Henle J, Simon P, Frenzel A, Scholz S, Kaskel S (2007) Nanosized BiOX (X = Cl, Br, I) particles synthesized in reverse microemulsions. Chem Mater 19:366–373
32. Lin X, Shan Z, Li K, Wang W, Yang J, Huang F (2007) Photocatalytic activity of a novel Bi-based oxychloride catalyst $Na_{0.5}Bi_{1.5}O_2Cl$. Solid State Sci 9:944–949
33. Zhai HF, Li AD, Kong JZ, Li XF, Zhao J, Guo BL, Yin J, Li Z (2013) Preparation and visible-light photocatalytic properties of $BiNbO_4$ and $BiTaO_4$ by a citrate method. J Solid State Chem 202:6–14
34. Kagata H, Inoue T, Kato J, Kameyama I (1992) Low-fire bismuth-based dielectric ceramics for microwave use. Jpn J Appl Phys 31:3152–3155
35. Choi W, Kim KY, Moon MR, Bae KS (1998) Effects of Nd_2O_3 on the microwave dielectric properties of $BiNbO_4$ ceramics. J Mater Res 13:2945–2949
36. Huang CL, Weng MH, Wu CC (2000) The microwave dielectric properties and the microstructures of la_2o_3-modified $BINBO_4$ ceramics. Jpn J Appl Phys 39:3506–3510
37. Tzou WC, Yang CF, Chen YC, Cheng PS (2000) Improvements in the sintering and microwave properties of $BiNbO_4$ microwave ceramics by V_2O_5 addition. J Eur Ceram Soc 20:991–996
38. Wang N, Zhao MY, Yin ZW, Li W (2003) Low-temperature synthesis of β-$BiNbO_4$ powder by citrate sol–gel method. Mater Lett 57:4009–4013
39. Wang N, Zhao MY, Yin ZW, Li W (2004) Effects of complex substitution of La and Nd for Bi on the microwave dielectric properties of $BiNbO_4$ ceramics. Mater Res Bull 39:439–448
40. Zhou D, Wang H, Yao X, Wei X, Xiang F, Pang L (2007) Phase transformation in ceramics. Appl Phys Lett 90:172910–172910–172910–172913
41. Xu C, He D, Liu C, Wang H, Zhang L, Wang P, Yin S (2013) High pressure and high temperature study the phase transitions of $BiNbO_4$. Solid State Commun 156:21–24
42. Lai K, Zhu Y, Dai Y, Huang B (2012) Intrinsic defect in $BiNbO_4$: a density functional theory study. J Appl Phys 112:043706–043706–043706–043709
43. Nisar J, Wang BC, Pathak B, Kang TW, Ahuja R (2011) Mo- and N-doped $BiNbO_4$ for photocatalysis applications. Appl Phys Lett 99: 051909–051909-3
44. Wang BC, Nisar J, Pathak B, Kang TW, Ahuja R (2012) Band gap engineering in $BiNbO_4$ for visible-light photocatalysis. Appl Phys Lett 100:182102–182102–182102–182104
45. Wong KM, Alay-e-Abbas SM, Shaukat A, Fang Y, Lei Y (2013) First-principles investigation of the size-dependent structural stability and electronic properties of O-vacancies at the ZnO polar and non-polar surfaces. J Appl Phys 113:014304–014304-11
46. Wong KM, Alay-e-Abbas, Fang Y, Shaukat A, Lei Y (2013) Spatial distribution of neutral oxygen vacancies on ZnO nanowire surfaces: an investigation combining confocal microscopy and first principles calculations. J Appl Phys 114:034901–034901-10
47. Perdew JP, Wang Y (1992) Accurate and simple analytic representation of the electron-gas correlation energy. Phys Rev B 45:13244–13249
48. Becke AD, Johnson ER (2006) A simple effective potential for exchange. J Chem Phys 124:221101–221101–221101–221104
49. Kuzmin A, Kalinko A, Evarestov RA (2013) Ab initio LCAO study of the atomic, electronic and magnetic structures and the lattice dynamics of triclinic $CuWO_4$. Acta Mater 61:371–378
50. Kubelka P, Munk F (1931) Ein Beitrag zur Optik Der Farban Striche. Z Tech Phys 12:593–603
51. Wiegel M, Middel W, Blasse G (1995) Influence of ns^2 ions on the luminescence of niobates and tantalates. J Mater Chem 5:981–983
52. Li AD, Zhai HF, Kong JZ, Wu D (2010) Ferroelectric and photocatalytical properties of ta-based and nb-based oxide ceramics and powders from environmentally friendly water-soluble tantalum and niobium precursors. Mater Sci Forum 654–656:2029–2032
53. Popolitov VI, Lobache AN, Peskin VF (1982) Antiferroelectrics, ferroelectrics and pyroelectrics of a stibiotantalite structure. Ferroelectrics 40:9–16
54. Tsujimi Y, Jangx MS, Yu YS, Yagi T (1994) The 90° brillouin scattering in β-$BiNbO_4$ single crystal. Ferroelectr Lett 17:33–39
55. Haddou A, Khachai H, Khenata R, Litimein F, Bouhemadou A, Murtaza G, Alahmed ZA, Bin-Omran S, Abbar B (2013) Elastic, optoelectronic, and thermal properties of cubic CSi_2N_4: an ab initio study. J Mater Sci 48:8235–8243